MDPI

# Dynamic Load Sharing Behavior for the Pitch Drive in MW Wind Turbines

Congfang Hu [1], Tao Yuan [1], Shiping Yang [1], Yunbo Hu [2] and Xiao Liang [1,*]

[1] School of Mechanical Engineering and Mechanics, Xiangtan University, Xiangtan 411105, China
[2] NFAIC High Precision Transmission Co., Ltd., Zhuzhou 412002, China
* Correspondence: liangxiao@xtu.edu.cn

**Abstract:** For a wind energy system, main speed-increasing gearboxes, pitch drives and yaw drives are composed of a multistage planetary gear system. However, inevitable errors in the manufacturing and assembling of the gears lead to uneven load of distribution in the planetary gear system; thus, its service life and reliability decrease greatly, which would eventually affect the normal operation of the whole wind power system. In this study, a dynamic load sharing model of pitch drive is established with a lumped-parameter method. Given the manufacturing and assembly errors and central floating gear, the dynamic equations for each component, the stiffness matrix and damping matrix, the dynamic load sharing coefficient and the floating displacement of the sun gear are obtained according to the dynamic meshing force and damping load. Furthermore, the load sharing coefficient for external and internal meshing of the pitch drive for a 2 MW wind turbine with a three-stage planetary gear are achieved. Then, the floating displacement of the sun gear and the displacement of other gears are also obtained. Moreover, the influence of both external and internal meshing stiffness, the eccentric error and tooth frequency error for all components on the load sharing coefficient of all stages are investigated. Lastly, the theoretical components displacement of this model is compared with experiment results of the pitch drive under 50%, 100% and 150% rated torque in a test rig; the correctness of the model is verified by the experiment results.

**Keywords:** wind energy; pitch drive; planetary gear system; load sharing; dynamics behavior

## 1. Introduction

A planetary gear is characterized by a high speed ratio, and its input torque is split into several parallel paths among planetary gears in the same stage, so its structure is more compact than others. Therefore, it is widely applied in fields such as aviation, automobile, wind turbine, etc. In addition, greater torque and smaller volume can be achieved by applying a multistage planetary gear system. All main gearboxes, pitch drives and yaw drives for the MW wind turbine comprise a multistage planetary system. However, unavoidable errors during the manufacture and assembling process cause unequal loads among the planetary gears and affect its reliability and operating life [1]. Therefore, it is essential to analyze load sharing characteristics of the planetary gearboxes in wind power systems.

Some researchers have investigated the load sharing of planetary gear systems. Iglesias et al. [2–4] considered the tangential and radial pin hole position error, fixed and floating central gears of a single-stage planetary gear system central gear floating. The results showed that the load sharing characteristics are better with the floating central gear, and the influence of the radial position error on the load sharing coefficient is larger than that of the tangential position error. Zhiliang Xu et al. [5] considered position errors of a gear pair. The results showed that suitable position errors can improve the load sharing condition by 10% if position errors change from 0.1 to 0.2 mm. Lokaditya Ryali et al. [6] established a dynamic load distribution model for a single-stage planetary gear system, and studied

the effect of system parameters such as meshing phase, tooth modifications and contact ratio on the dynamic characteristics of the system. Kim et al. [7,8] analyzed the impact of increasing torque and rotation direction changing on the dynamic load sharing performance of planetary gearboxes through experiments. It showed that the increasing torque can improve the load sharing characteristics. Jungang Wang et al. [9] established a dynamics model for a multistage planetary gear system to study the load-sharing performance under the interaction of random input speed and internal excitation. The results showed that the fluctuation of the load sharing coefficient in the first-stage is more intense; thus, it is necessary to improve load distribution among gear pairs in the first-stage, which reduces vibration and prolongs the life.

Furthermore, some studies focused on load sharing measures to reduce the uneven load distribution. Julian Theling et al. [10] presented a method which combines a structural optimization with tooth contact analysis for planetary gearboxes. The results showed that the optimized geometry is capable of reducing the excitation and improving the load sharing behavior. Woo-Jin Chung et al. [11] analytically investigated the effects of floating components on the load sharing characteristics and the strength of planetary gearboxes with non-torque load and carrier pinhole position errors. The results implied that the load sharing characteristics of planetary gearboxes are improved by floating components. Zhixin Fan et al. [12] focused on flexible ring gears based on shell and Timoshenko beam theory. The results indicated that the flexible ring gear sharply reduces dynamic loads and uneven load distribution of the system. Lokaditya Ryali et al. [13] combined finite element input/output shafts and carrier in a computational model of planetary gear sets. The results showed that flexible carriers improve the load sharing among planetary gears.

In addition, other researchers also explored the dynamic characteristics and load distribution of planetary gear systems in a wind turbine gearbox. Young-Jun Park et al. [14] used a 1/4 scale-down model of a main speed increasing gearbox for a 2-MW wind turbine and conducted a parametric study with a three-dimensional model. The results of the analysis showed that the radial force and moment were major non-torque elements that affect the load sharing of planet gears. Magnitudes, positions and phases of pinhole position errors also affect the load sharing characteristics of the planet gears significantly. When non-torque loads and pinhole position errors acted together, the influence of pinhole position errors was greater than that of the non-torque loads. Ho-gil Yoo et al. [15] designed a flexible pin to improve load sharing of the main speed increasing gearbox for a wind turbine gearbox. The results showed that the load sharing performance improved significantly with the flexible pin. Additionally, the flexible pin design ensured that all components satisfied the strength requirement.

However, all the above studies are related to the load sharing behavior of the main speed increasing gearboxes in wind turbines; there are few studies focused on the pitch drive in wind turbines. Accordingly, it is necessary to investigate the load sharing performance of the planetary gear system of the pitch drive in wind power systems. In this study, a lumped-parameter model for a pitch drive is developed to explore the dynamic load sharing characteristics. This article is organized as follows: In Section 2, the dynamic load sharing model of planetary gear systems is briefly introduced. Section 3 analyzes the dynamic load sharing coefficient and displacement of a pitch drive with a three-stage planetary gear system and discusses the impact of meshing stiffness, eccentric errors and tooth frequency errors in the load sharing behaviors. A comparison of the theoretical dynamics behavior and the experiment result is set out in Section 4.

## 2. Dynamic Load Sharing Model of the Pitch Drive for the MW Wind Turbine

The pitch drive consists of several stages of a planetary gear system connected in series. Each stage is composed of a sun gear, planetary gears, a ring gear and a carrier. The power of the pitch drive is inputted from the sun gear in the first stage and transferred through planetary gears to the carrier, which is connected to the sun gear in next stage by splines. The power is outputted to the carrier in the last stage. Consequently, mutual

supports are created between the sun gear in the next stage and the front carrier. Figure 1 shows the three-dimensional structure of a three-stage planetary gear system, and Figure 2 shows how they are connected.
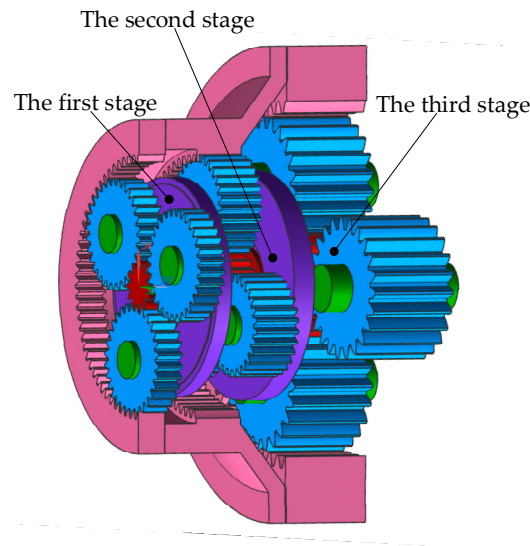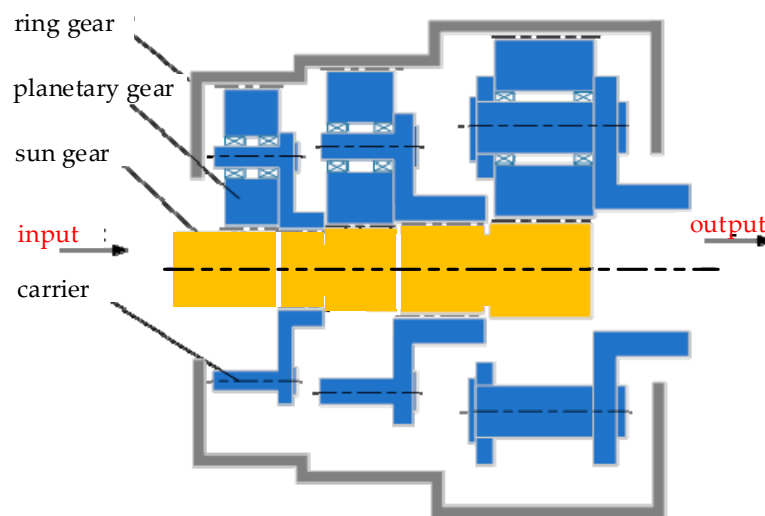


**Figure 1.** The three dimension structure.



**Figure 2.** The connection of the planetary gear system.

### 2.1. Lumped-Parameter Model of the Planetary System for MW Wind Turbines

The lumped-parameter dynamics model of a single-stage planetary gear system is shown in Figure 3. In this model, as its main components are considered rigid, the gear meshing is modeled as a spring with time-varying stiffness, a damping and an equivalent error along the meshing line, where the equivalent error is connected with the spring and damping in parallel. Additionally, other supporting springs are linear. In the same stage, all planetary gears are assumed to be identical with the mass, inertia, gear profile error and gear meshing stiffness. However, the mass, inertia, gear profile error and gear meshing stiffness of planetary gears in different stages are not the same. $H_j$-$O_j$-$V_j$, $\xi_{ij}$-$O_{ij}$-$\eta_{ij}$ and $X_j$-$O_j$-$Y_j$ represent the coordinates of the sun gear, the $i^{th}$ planetary gear and the carrier in the $j^{th}$ stage, respectively. The axial displacement of all the components is not taken into consideration.
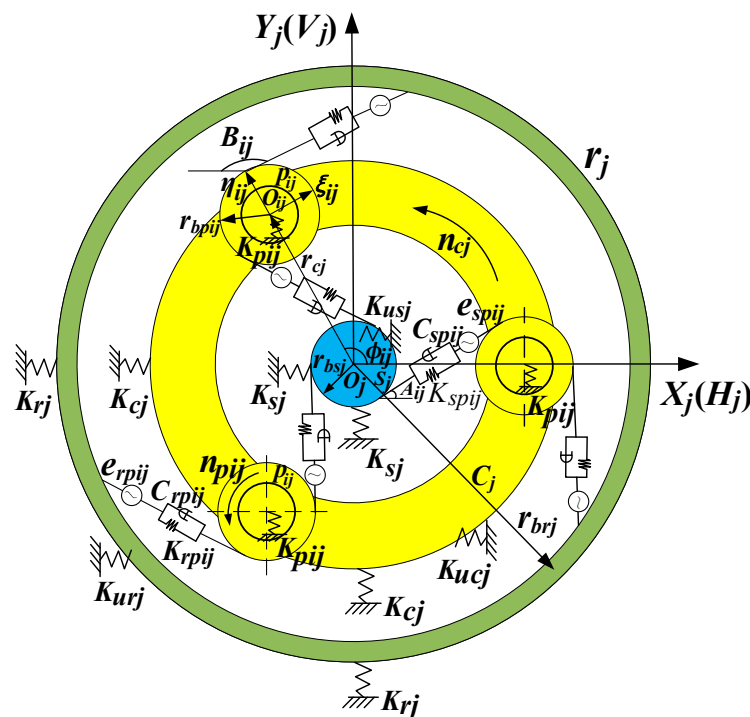
**Figure 3.** The dynamics model of the planetary gear system in the $j$th stage.

In Figure 3, $K_{sj}$, $K_{rj}$, $K_{pij}$ and $K_{cj}$ represent the support stiffness of the sun gear, ring gear, $i$th planetary gear and the carrier in $j$th stage, respectively, and $K_{usj}$, $K_{urj}$, $K_{ucj}$ are the rotational stiffness of the sun gear, the ring gear and carrier, respectively. The meshing between the sun gear and the planetary gear is defined as external meshing, and that between the ring gear and the planetary gear is defined as internal meshing. $K_{spij}$ and $K_{rpij}$ are the stiffness of the external meshing and the internal meshing, respectively. $C_{spij}$ and $C_{rpij}$ are the damping of the external meshing and the internal meshing, respectively. $e_{spij}$ and $e_{rpij}$ are the equivalent error of the external meshing and the internal meshing, respectively. $u_{pij}$, $u_{sj}$ and $u_{cj}$ are the rotational displacement of the planetary gear, the sun gear and the carrier in the $j$th stage, respectively. $u_{sj} = r_{bsj} \times \theta_{sj}$, $u_{pij} = r_{bpij} \times \theta_{pij}$, and $u_{cj} = r_{cj} \times \theta_{cj}$.

*2.2. Errors in the Model*

2.2.1. Manufacturing and Assembling Errors

Because of the manufacturing and assembling errors, the load is not equally shared among the planetary gears of the planetary gear system. The considered manufacturing errors in this paper are the eccentric error and tooth frequency error.

When the previous meshing for the tooth pair ends and the next meshing starts, the tooth profile deviation and the base pitch error of the gear cause the load varying along the meshing line. These two types of errors are defined as the tooth frequency error, so it is necessary to consider the influence of the tooth frequency error $\varepsilon_{spij}$ on the dynamic load sharing. The tooth frequency error $\varepsilon_{spij}$ of the external meshing and $\varepsilon_{rpij}$ of the internal meshing are valued by their tolerance.

Moreover, the assembling error is only considered for the ring gear for the floating carrier and sun gear. The eccentric and assembling errors considered in this study are shown in Table 1. The symbols E and A represent the manufacturing error and assembling error, respectively. $\beta_{sj}$, $\beta_{pj}$, $\beta_{cj}$, and $\beta_{rj}$ are the phase angles of the manufacturing error $E$ for the sun gear, the planetary gear, the carrier and the ring gear, respectively. $\gamma_{rj}$ is the phase angle of the assembly error $A_{rj}$.

**Table 1.** Manufacturing and assembling error for the components.

| Part | Error | Symbol | Phase Angle |
|---|---|---|---|
| Sun gear | eccentric error | $E_{sj}$ | $\beta_{sj}$ |
| Planetary Gear | eccentric error | $E_{pj}$ | $\beta_{pj}$ |
| Carrier | planetary pin hole error | $E_{cj}$ | $\beta_{cj}$ |
| Ring gear | eccentric error | $E_{rj}$ | $\beta_{rj}$ |
| | assembling error | $A_{rj}$ | $\gamma_{rj}$ |

2.2.2. Equivalent Meshing Error

The meshing error consists of the above manufacturing and assembly errors of different components. Thus, it is vital to determine the equivalent meshing error by transforming these errors along the meshing line [16]. The equivalent meshing error $e_{spij}$ between the sun gear and the $i^{th}$ ($i = 1, 2, \ldots$, n) planetary gear and the meshing error $e_{rpij}$ between the ring gear and the $i^{th}$ planetary gear are calculated as follows:

$$
\begin{cases}
e_{spij} = -E_{sj}\sin\left[(\omega_{sj} - \omega_{cj})t + \beta_{sj} + \alpha_{wj} - \varphi_{ij}\right] - E_{pij}\sin\left[(\omega_{pj} - \omega_{cj})t + \beta_{pij} + \alpha_{wj}\right] \\
\qquad + E_{cj}\sin(\beta_{cj} - \varphi_{ij})\cos\alpha_{wj} + \varepsilon_{spij} \\
e_{rpij} = E_{rj}\sin(-\omega_{cj}t + \beta_{rj} - \alpha_{rj} - \varphi_{ij}) + E_{pij}\sin\left[(\omega_{pj} - \omega_{cj})t + \beta_{pij} - \alpha_{nj}\right] \\
\qquad - E_{cj}\sin(\beta_{cj} - \varphi_{ij})\cos\alpha_{nj} + A_{rj}\sin(-\omega_{cj}t + \gamma_{rj} - \alpha_{nj} - \varphi_{ij}) + \varepsilon_{ppij}
\end{cases}
\tag{1}
$$

where $\omega_{sj}$, $\omega_{cj}$ and $\omega_{pj}$ are the angular velocities of the sun gear, the carrier and the planetary gear in the $j^{th}$ stage, respectively. $\varphi_{ij}$ is the phase angle of the $i^{th}$ planetary gear in the $j^{th}$ stage, $\varphi_{ij} = 2\pi(j-1)/n$. $\alpha_{wj}$ and $\alpha_{nj}$ are the external and internal meshing angles in the $j^{th}$ stage, respectively. $\varepsilon_{spij}$ is the tooth frequency error of the external meshing gear, and $\varepsilon_{rpij}$ is the tooth frequency error of the internal meshing gear.

2.2.3. Floating Error

The radial flotation of the central member causes the displacement varying along the internal and external meshing lines in the planetary gear system, so the floating displacement also needs to be transformed into the floating error [17]. $H_{sj}$ and $V_{sj}$ are the floating displacements of the sun gear in the horizontal and vertical directions in the $H_j$-$O_j$-$V_j$ coordinates, respectively. $X_{cj}$ and $Y_{cj}$ are the floating displacements for the carrier in the horizontal and vertical directions in the $X_j$-$O_j$-$Y_j$ coordinates, respectively. The ring gear is fixed, so its displacement is zero. The floating displacements $H_{sj}$ and $V_{sj}$ of the sun gear are incorporated in the floating error $\Delta_{sij}$ of the external meshing, and $X_{cj}$ and $Y_{cj}$ are incorporated in the floating error $\Delta_{cisj}$ of the external meshing and incorporated in the floating error $\Delta_{cirj}$ of the internal meshing. These errors are indicated as below:

$$
\begin{cases}
\Delta_{sij} = H_{sj}\cos A_{ij} + V_{sj}\sin A_{ij} \\
\Delta_{cisj} = X_{cj}\cos A_{ij} + Y_{cj}\sin A_{ij} \\
\Delta_{cirj} = X_{cj}\cos B_{ij} + Y_{cj}\sin B_{ij}
\end{cases}
\tag{2}
$$

where $A_{ij}$ represents the azimuth angle of the meshing line between the sun gear and the $i^{th}$ planetary gear, $A_{ij} = \omega_{cj}t + \pi/2 - \alpha_{wj} + \varphi_{ij}$, and $B_{ij}$ represents the azimuth angle of the meshing line between the $i^{th}$ planetary gear and the ring gear, $B_{ij} = \omega_{cj}t + \pi/2 + \alpha_{nj} + \varphi_{ij}$.

*2.3. Dynamic Load and Damping Force along the Meshing Line*

All the time-varying meshing stiffness [18], the equivalent meshing error, the floating error and the tooth frequency error of planetary gears are considered in the dynamic load

sharing model of the pitch drive. The dynamic load $W_{\text{spij}}$ of the external meshing and $W_{\text{rpij}}$ of the internal meshing are presented as follows:

$$
\begin{cases}
W_{spij} = K_{spij}(t)\cdot(x_{sj} - x_{pij} - \xi_{pj}\sin\alpha_{wj} - \eta_{pj}\cos\alpha_{wj} - e_{spij} - \Delta_{sij} - \Delta_{cisj}) \\
W_{rpij} = K_{rpij}(t)\cdot(x_{pij} + \xi_{pj}\sin\alpha_{nj} + \eta_{pj}\cos\alpha_{nj} - e_{rpij} - \Delta_{rij} - \Delta_{cisj})
\end{cases}
\tag{3}
$$

where $K_{\text{spij}}$ is the time-varying stiffness of the external meshing, and $K_{\text{rpij}}$ is the time-varying stiffness of the internal meshing.

The time-varying meshing stiffness can be approximately expressed by the Fourier series expansion as follows [17]:

$$
k(t) = k_o + \frac{k_{\max} - k_{\min}}{2}\sum_{n=1}^{N}\frac{4}{\pi n}(-1)^{-1}\sin n[(ICR - 2)\pi]\cos n\omega_c t
\tag{4}
$$

where $k_o$ is the average meshing stiffness of the gear pair, $k_{\min}$ is the meshing stiffness of a single tooth pair and $k_{\max}$ is the meshing stiffness of double tooth pairs. ICR is the contact ratio of the gear pair and $\omega$ is the meshing frequency.

By substituting the Equations (1) and (2) into the Equation (3), the dynamic meshing force of the external and internal meshing can be calculated as follows:

$$
\begin{cases}
\begin{aligned}
W_{spij} =\, & K_{spij}(t)\cdot\big\{x_{sj} - x_{pij} - \xi_{pj}\sin\alpha_{wj} - \eta_{pj}\cos\alpha_{wj} + H_{sj}\sin(\varphi_{ij} - \alpha_{wj}) - V_{sj}\cos(\varphi_{ij} - \alpha_{wj}) \\
& + X_{cj}\sin(\varphi_{ij} - \alpha_{wj}) - Y_{cj}\cos(\varphi_{ij} - \alpha_{wj}) + E_{sj}\sin[(\omega_{sj} - \omega_{cj})t + \beta_{sj} + \alpha_{wj} - \varphi_{ij}] \\
& + E_{pj}\sin[(\omega_{pj} - \omega_{cj})t + \beta_{pj} + \alpha_{wj}] - E_{cj}\sin(\beta_{cj} - \varphi_{ij})\cos\alpha_{wj} - \varepsilon_{spij}\big\} \\
W_{rpij} =\, & K_{rpij}(t)\cdot\big\{x_{pij} + \xi_{pj}\sin\alpha_{pj} + \eta_{pj}\cos\alpha_{pj} + X_{cj}\sin(\varphi_{ij} - \alpha_{nj}) - Y_{cj}\cos(\varphi_{ij} - \alpha_{nj}) \\
& - E_{rj}\sin(-\omega_{cj}t + \beta_{rj} - \alpha_{nj} - \varphi_{ij}) - E_{pj}\sin[(\omega_{pj} - \omega_{cj})t + \beta_{pj} - \alpha_{pj}] \\
& + E_{cj}\sin(\beta_{cj} - \varphi_{ij})\cos\alpha_{nj} + A_{rj}\sin(-\omega_{cj}t + \gamma_{rj} - \alpha_{nj} - \varphi_{ij}) - \varepsilon_{rpij}\big\}
\end{aligned}
\end{cases}
\tag{5}
$$

Corresponding to $W_{\text{spij}}$ and $W_{\text{rpij}}$, the damping force $D_{\text{spij}}$ of the external meshing and $D_{\text{rpij}}$ of the internal meshing are the following:

$$
\begin{cases}
\begin{aligned}
D_{spij} =\, & C_{spij}\big\{\dot{x}_{sj} - \dot{x}_{pij} - \dot{\xi}_{pj}\sin\alpha_{wj} - \dot{\eta}_{pj}\cos\alpha_{wj} + \dot{H}_{sj}\sin(\varphi_{ij} - \alpha_{wj}) - \dot{V}_{sj}\cos(\varphi_{ij} - \alpha_{wj}) \\
& + \dot{X}_{cj}\sin(\varphi_{ij} - \alpha_{wj}) - \dot{Y}_{cj}\cos(\varphi_{ij} - \alpha_{wj}) + E_{sj}\omega_{cj}\cos[(\omega_{sj} - \omega_{cj})t + \beta_{sj} + \alpha_{wj} - \varphi_{ij}] \\
& + E_{pj}\omega_{cj}\cos[(\omega_{pj} - \omega_{cj})t + \beta_{pj} + \alpha_{wj}] - E_{cj}\omega_{cj}\sin(\beta_{cj} - \varphi_{ij})\cos\alpha_{wj})\big\} \\
D_{rpij} =\, & C_{rpij}\big\{\dot{x}_{pij} + \dot{\xi}_{pj}\sin\alpha_{nj} + \eta_{pj}\cos\alpha_{nj} + \dot{X}_{cj}\sin(\varphi_{ij} - \alpha_{nj}) - \dot{Y}_{cj}\cos(\varphi_{ij} - \alpha_{nj}) \\
& - E_{rj}\omega_{cj}\sin(-\omega_{cj}t + \beta_{rj} - \alpha_{nj} - \varphi_{ij}) - E_{pj}\omega_{cj}\sin[(\omega_{pj} - \omega_{cj})t + \beta_{pj} - \alpha_{nj}] \\
& + E_{cj}\omega_{cj}\sin(\beta_{cj} - \varphi_{ij})\cos\alpha_{nj} + A_{rj}\omega_{cj}\cos(-\omega_{cj}t + \gamma_{rj} - \alpha_{nj} - \varphi_{ij})\big\}
\end{aligned}
\end{cases}
\tag{6}
$$

where $K_{\text{spij}}$ and $K_{\text{rpij}}$ are the time-varying stiffness of the external and internal meshing, respectively, and $C_{\text{spij}}$ and $C_{\text{rpij}}$ are the damping coefficients of the external and internal meshing, respectively.

The damping coefficient $C_{\text{spij}}$ of the external meshing and the damping coefficient $C_{\text{rpij}}$ of the internal meshing are the following:

$$
C_{spij} = 2\varsigma\sqrt{\frac{K_{spij}}{1/m_{pij} + 1/m_{sj}}}
\tag{7}
$$

$$
C_{rpij} = 2\varsigma\sqrt{\frac{K_{rpij}}{1/m_{pij} + 1/m_{rj}}}
\tag{8}
$$

where $\zeta$ is the damping ratio, which is 0.007 for steel, and $m_{\text{sj}}$, $m_{\text{pij}}$, and $m_{\text{rj}}$ are the mass of the sun gear, the $i^{\text{th}}$ planetary gear and the ring gear, respectively.

### 2.4. Dynamics Model of the Planetary Gear System

The dynamics model of the system is

$$M\ddot{x} + C\dot{x} + Kx = P \tag{9}$$

For the pitch drive, the displacement vector is as follows:

$$
\begin{aligned}
x = \ & [u_{s1}, u_{p11}, \xi_{p11}, \eta_{p11}, u_{p21}, \xi_{p21}, \eta_{p21}, \ldots, u_{pi1}, \xi_{pi1}, \eta_{pi1}, u_{c1}, X_{c1}, Y_{c1}, \\
& u_{s2}, H_{s2}, V_{s2}, u_{p12}, \xi_{p12}, \eta_{p12}, u_{p22}, \xi_{p22}, \eta_{p22}, \ldots, u_{pi2}, \xi_{pi2}, \eta_{pi2}, u_{c2}, X_{c2}, Y_{c2}, \ldots \\
& u_{sj}, H_{sj}, V_{sj}, u_{p1j}, \xi_{p1j}, \eta_{p1j}, u_{p2j}, \xi_{p2j}, \eta_{p2j}, \ldots, u_{pij}, \xi_{pij}, \eta_{pij}, u_{cj}, X_{cj}, Y_{cj}]^T
\end{aligned} \tag{10}
$$

The mass matrix $M$ for the system is the following:

$$
\begin{aligned}
M = \mathrm{diag} \Bigg[ & \frac{I_{s1}}{r_{bs1}^2}, \frac{I_{p11}}{r_{bp11}^2}, m_{p11}, m_{p11}, \frac{I_{p21}}{r_{bp21}^2}, m_{p21}, m_{p21}, \ldots, \frac{I_{pi1}}{r_{bpi1}^2}, m_{pi1}, m_{pi1}, \frac{I_{c1}}{r_{bc1}^2}, m_{c1}, m_{c1}, \\
& \frac{I_{s2}}{r_{bs2}^2}, m_{s2}, m_{s2}, \frac{I_{p12}}{r_{bp12}^2}, m_{p12}, m_{p12}, \frac{I_{p22}}{r_{bp22}^2}, m_{p22}, m_{p22}, \ldots, \frac{I_{pi2}}{r_{bpi2}^2}, m_{pi2}, m_{pi2}, \frac{I_{c2}}{r_{bc2}^2}, m_{c2}, m_{c2}, \ldots \\
& \frac{I_{sj}}{r_{bsj}^2}, m_{sj}, m_{sj}, \frac{I_{p1j}}{r_{bp1j}^2}, m_{p1j}, m_{p1j}, \frac{I_{p2j}}{r_{bp2j}^2}, m_{p2j}, m_{p2j}, \ldots, \frac{I_{pij}}{r_{bpij}^2}, m_{pij}, m_{pij}, \frac{I_{cj}}{r_{bq}^2}, m_{cj}, m_q \Bigg]
\end{aligned} \tag{11}
$$

where $m_{sj}$ is the mass of the sun gear in the $j$th stage, $m_{pij}$ is the mass of the $i$th planetary gear in the $j$th stage, and $m_{rj}$ is the carrier mass in the $j$th stage.

For each stage, the dynamic equation [19] for the sun gear, the planetary gears and the carrier in the translation and torsional directions are deduced as follows:

The sun gear:

$$
\begin{cases}
\dfrac{I_{sj}}{r_{bsj}^2}\ddot{x}_{sj} + \sum\limits_{i=1}^{n}(D_{spij} + W_{spij}) = T/r_{bsj} \\[2mm]
m_{sj}\ddot{H}_{sj} + \sum\limits_{i=1}^{n}(D_{spij} + W_{spij})\sin(\varphi_{ij} - a_{wj}) = 0 \\[2mm]
m_{sj}\ddot{V}_{sj} - \sum\limits_{i=1}^{n}(D_{spij} + W_{spij})\cos(\varphi_{ij} - a_{wj}) = 0
\end{cases} \tag{12}
$$

The $i$th planetary gear:

$$
\begin{cases}
\dfrac{I_{pij}}{r_{bpij}^2}\ddot{x}_{pij} - (D_{spij} + W_{spij}) + (D_{rpij} + W_{rpij}) = 0 \\[2mm]
m_{pij}\ddot{\xi}_{pij} - (D_{spij} + W_{spij})\sin a_{wj} + (D_{rpij} + W_{rpij})\sin a_{nj} + K_{pij}\xi_{ij} = 0 \\[2mm]
m_{pij}\ddot{\eta}_{pij} - (D_{spij} + W_{spij})\cos a_{wj} + (D_{rpij} + W_{rpij})\cos a_{nj} + K_{pij}(\eta_{Pij} - x_{cj}) = 0
\end{cases} \tag{13}
$$

The carrier:

$$
\begin{cases}
\dfrac{I_{cj}}{r_{bcj}^2}\ddot{x}_{cj} + \sum\limits_{i=1}^{n}(x_{cj} - \eta_{pij})K_{pij} + K_{ucj}x_{cj} = 0 \\[2mm]
m_{cj}\ddot{X}_{cj} + \sum\limits_{i=1}^{n}(D_{spij} + W_{spij})\sin(\varphi_{ij} - a_{wj}) + \sum\limits_{i=1}^{n}(D_{rpij} + W_{rpij})\sin(\varphi_{ij} - a_{nj}) + K_{cj}X_{cj} = 0 \\[2mm]
m_{cj}\ddot{Y}_{cj} - \sum\limits_{i=1}^{n}(D_{spij} + W_{spij})\cos(\varphi_{ij} - a_{wj}) - \sum\limits_{i=1}^{n}(D_{rpij} + W_{rpij})\cos(\varphi_{ij} - a_{nj}) + K_{cj}Y_{cj} = 0
\end{cases} \tag{14}
$$

where: $T$ is the input torque of the sun gear, $K_{pij}$ is the support stiffness of the $i$th planetary gear, $K_{ucj}$ is the torsion stiffness of the spline and $K_{cj}$ is the support stiffness of the carrier.

Based on dynamic equations, the stiffness matrix $K_j$ for the whole planetary gear system in the $j^{\text{th}}$ stage is shown in Equation (15).

$$K_j = \begin{bmatrix} K_{sj} & K_{spij} & K_{scj} \\ K_{spij} & diag K_{pij} & K_{cpij} \\ K_{scj} & K_{cpij} & K_{cj} \end{bmatrix} \tag{15}$$

$$K_{sj} = K_{spij} \begin{bmatrix} n & -\sum_{i=1}^{n} \sin \eta_{ij} & \sum_{i=1}^{n} \cos \eta_{ij} \\ -\sum_{i=1}^{n} \sin \eta_{ij} & K_{1j} + \sum_{i=1}^{n} \sin^2(\varphi_i - a_w) & -\sum_{i=1}^{n} \cos \eta_{ij} \sin \eta_{ij} \\ \sum_{i=1}^{n} \cos \eta_{ij} & -\sum_{i=1}^{n} \cos \eta_{ij} \sin \eta_{ij} & K_{1j} + \sum_{i=1}^{n} \cos^2 \eta_{ij} \end{bmatrix}$$

$$K_{spij} = K_{spij} \begin{bmatrix} 1 + K_{2j} & \sin a_{wj} + K_{2j} \sin a_{nj} & \cos a_{wj} + K_{2j} \cos a_{nj} \\ \sin a_{wj} + K_{2j} \sin a_{nj} & K_{3j} + \sin^2 a_{wj} + K_{2j} \sin^2 a_{nj} & \sin a_{wj} \cos a_{wj} + K_{2j} \sin a_{nj} \cos a_{nj} \\ \cos a_{wj} + K_{2j} \cos a_{nj} & \sin a_{wj} \cos a_{wj} + K_{2j} \sin a_{nj} \cos a_{nj} & K_{3j} + \cos^2 a_{wj} + K_{2j} \cos^2 a_{nj} \end{bmatrix}$$

$$K_{cj} = K_{spij} \begin{bmatrix} nK_{3j} + K_{4j} & 0 & 0 \\ 0 & \sum_{i=1}^{n} \sin^2 \eta_{ij} + \sum_{i=1}^{n} K_{2j} \sin^2 \xi_{ij} + K_{cj} & -\sum_{i=1}^{n} \cos \eta_{ij} \sin \eta_{ij} - \sum_{i=1}^{n} K_{2j} \cos \xi_{ij} \sin \xi_{ij} \\ 0 & -\sum_{i=1}^{n} \cos \eta_{ij} \sin \eta_{ij} - \sum_{i=1}^{n} K_{2j} \cos \xi_{ij} \sin \xi_{ij} & \sum_{i=1}^{n} K_{spij} \cos^2 \eta_{ij} + \sum_{i=1}^{n} K_{2j} \cos^2 \xi_{ij} + K_{5j} \end{bmatrix}$$

$$K_{sipj} = K_{spij} \begin{bmatrix} -1 & -\sin \eta_{ij} & -\cos \eta_{ij} \\ -\sin \eta_{ij} & -\sin \eta_{ij} \sin \alpha_{wj} & -\cos \eta_{ij} \sin \alpha_{wj} \\ \cos \eta_{ij} & \cos \eta_{ij} \sin \alpha_{wj} & \cos \eta_{ij} \cos \alpha_{wj} \end{bmatrix}$$

$$K_{cpij} = K_{spij} \begin{bmatrix} 0 & -\sin \eta_{ij} + K_{2j} \sin \xi_{ij} & \cos \eta_{ij} - K_{2j} \cos \xi_{ij} \\ 0 & -\sin \eta_{ij} \sin \alpha_{wj} + K_{2j} \sin \xi_{ij} \sin a_{nj} & \cos \eta_{ij} \sin \alpha_{wj} + K_{2j} \sin \xi_{ij} \sin a_{nj} \\ -K_{3j} & -\sin \eta_{ij} \cos \alpha_{wj} + K_{2j} \sin \xi_{ij} \cos \alpha_{nj} & \cos \eta_{ij} \cos \alpha_{wj} + K_{2j} \cos \xi_{ij} \cos \alpha_{nj} \end{bmatrix}$$

$$K_{scj} = K_{spij} \begin{bmatrix} 0 & \sum_{i=1}^{n} \sin \eta_{ij} & -\sum_{i=1}^{n} \cos \eta_{ij} \\ 0 & \sum_{i=1}^{n} \sin^2 \eta_{ij} & -\sum_{i=1}^{n} \cos \eta_{ij} \sin \eta_{ij} \\ 0 & -\sum_{i=1}^{n} \cos \eta_{ij} \sin \eta_{ij} & -\sum_{i=1}^{n} \cos^2 \eta_{ij} \end{bmatrix}$$

where $\eta_{ij} = \varphi_{ij} - \alpha_{wj}$, $\xi_{ij} = \varphi_{ij} - \alpha_{nj}$, $K_{1j} = K_{sj}/K_{spij}$, $K_{2j} = K_{rpij}/K_{spij}$, $K_{3j} = K_{pij}/K_{spij}$, $K_{4j} = K_{ucj}/K_{spij}$, and $K_{5j} = K_{cj}/K_{spij}$.

Similar to the stiffness matrix, the overall damping matrix $C_j$ of the whole planetary gear system in the $j^{\text{th}}$ stage is shown in Equation (16).

$$C_j = \begin{bmatrix} C_{sj} & C_{spij} & C_{scj} \\ C_{spij} & diag C_{pij} & C_{cpij} \\ C_{scj} & C_{cpij} & C_{cj} \end{bmatrix} \tag{16}$$

Each sub-matrix of the damping matrix $C_j$ of the planetary gear system in the $j^{\text{th}}$ stage in Equation (16) is shown as follows:

$$C_{sj} = C_{spij} \begin{bmatrix} n & -\sum_{i=1}^{n} \sin \eta_{ij} & \sum_{i=1}^{n} \cos \eta_{ij} \\ -\sum_{i=1}^{n} \sin \eta_{ij} & C_{1j} + \sum_{i=1}^{n} \sin^2(\varphi_i - a_w) & -\sum_{i=1}^{n} \cos \eta_{ij} \sin \eta_{ij} \\ \sum_{i=1}^{n} \cos \eta_{ij} & -\sum_{i=1}^{n} \cos \eta_{ij} \sin \eta_{ij} & C_{1j} + \sum_{i=1}^{n} \cos^2 \eta_{ij} \end{bmatrix}$$

$$
C_{spij} = C_{spij} \begin{bmatrix} 1 + C_{1j} & \sin a_{wj} + C_{1j} \sin a_{nj} & \cos a_{wj} + C_{1j} \cos a_{nj} \\ \sin a_{wj} + C_{1j} \sin a_{nj} & \sin^2 a_{wj} + C_{1j} \sin^2 a_{nj} & \sin a_{wj} \cos a_{wj} + C_{1j} \sin a_{nj} \cos a_{nj} \\ \cos a_{wj} + C_{1j} \cos a_{nj} & \sin a_{wj} \cos a_{wj} + K_{2j} \sin a_{nj} \cos a_{nj} & \cos^2 a_{wj} + C_{1j} \cos^2 a_{nj} \end{bmatrix}
$$

$$
C_{cj} = C_{spij} \begin{bmatrix} 0 & 0 & 0 \\ 0 & \sum_{i=1}^{n} \sin^2 \eta_{ij} + \sum_{i=1}^{n} C_{1j} \sin^2 \xi_{ij} + K_{cj} & -\sum_{i=1}^{n} \cos \eta_{ij} \sin \eta_{ij} - \sum_{i=1}^{n} C_{1j} \cos \xi_{ij} \sin \xi_{ij} \\ 0 & -\sum_{i=1}^{n} \cos \eta_{ij} \sin \eta_{ij} - \sum_{i=1}^{n} C_{1j} \cos \xi_{ij} \sin \xi_{ij} & \sum_{i=1}^{n} K_{spij} \cos^2 \eta_{ij} + \sum_{i=1}^{n} C_{1j} \cos^2 \xi_{ij} + K_{5j} \end{bmatrix}
$$

$$
C_{sipj} = C_{spij} \begin{bmatrix} -1 & -\sin \eta_{ij} & -\cos \eta_{ij} \\ -\sin \eta_{ij} & -\sin \eta_{ij} \sin \alpha_{wj} & -\cos \eta_{ij} \sin \alpha_{wj} \\ \cos \eta_{ij} & \cos \eta_{ij} \sin \alpha_{wj} & \cos \eta_{ij} \cos \alpha_{wj} \end{bmatrix}
$$

$$
C_{cpij} = C_{spij} \begin{bmatrix} 0 & -\sin \eta_{ij} + C_{1j} \sin \xi_{ij} & \cos \eta_{ij} - C_{1j} \cos \xi_{ij} \\ 0 & -\sin \eta_{ij} \sin \alpha_{wj} + C_{1j} \sin \xi_{ij} \sin a_{nj} & \cos \eta_{ij} \sin \alpha_{wj} + C_{1j} \sin \xi_{ij} \sin a_{nj} \\ 0 & -\sin \eta_{ij} \cos \alpha_{wj} + C_{1j} \sin \xi_{ij} \cos \alpha_{nj} & \cos \eta_{ij} \cos \alpha_{wj} + C_{1j} \cos \xi_{ij} \cos \alpha_{nj} \end{bmatrix}
$$

$$
C_{scj} = C_{spij} \begin{bmatrix} 0 & \sum_{i=1}^{n} \sin \eta_{ij} & -\sum_{i=1}^{n} \cos \eta_{ij} \\ 0 & \sum_{i=1}^{n} \sin^2 \eta_{ij} & -\sum_{i=1}^{n} \cos \eta_{ij} \sin \eta_{ij} \\ 0 & -\sum_{i=1}^{n} \cos \eta_{ij} \sin \eta_{ij} & -\sum_{i=1}^{n} \cos^2 \eta_{ij} \end{bmatrix}
$$

where $C_{1j} = C_{rpj}/C_{spj}$.

Then, the overall stiffness matrix and the damping matrix of the pitch drive are integrated by the stiffness matrix and the damping matrix of each stage, which are as follows:

$$
K = \begin{bmatrix} K_1 & & \\ & \ddots & \\ & & K_j \end{bmatrix} \tag{17}
$$

$$
C = \begin{bmatrix} C_1 & & \\ & \ddots & \\ & & C_j \end{bmatrix} \tag{18}
$$

### 2.5. Dynamic Load Sharing Coefficient and Sun Gear Floating Displacement

The dynamic load sharing coefficient indicates an unequal degree of the load sharing among planetary gears in the system. The larger the load sharing coefficient is, the more uneven load sharing is then indicated. The displacement vector $u$ can be obtained through numerical solution of the differential Equation (9) with the Runge–Kutta method. Then, the dynamic load can be achieved by substituting the displacements into Equation (5).

With both the external meshing and internal meshing load for each planetary gear, the load sharing coefficient for the external and internal meshing is able to be obtained separately. The tooth frequency cycle is defined as the period when the sun gear rotates one tooth. In the $k^{th}$ tooth frequency cycle, the load sharing coefficient $B_{spij}$ of the external meshing and $B_{rpij}$ of the internal meshing of the $i^{th}$ planetary gear in the $j^{th}$ stage can be obtained with the maximum dynamic load:

$$
\begin{cases} B_{spij} = n \cdot \max_{\substack{1 \le i \le n \\ 1 \le k \le t_1}} (W_{spijk}) / \sum_{i=1}^{n} \max_{\substack{1 \le i \le n \\ 1 \le k \le t_1}} (W_{spijk}) \\ B_{rpij} = n \cdot \max_{\substack{1 \le i \le n \\ 1 \le k \le t_1}} (W_{rpijk}) / \sum_{i=1}^{n} \max_{\substack{1 \le i \le n \\ 1 \le k \le t_1}} (W_{rpijk}) \end{cases} \tag{19}
$$

In the whole operating process, the dynamic load sharing coefficients $B_{spj}$ and $B_{rpj}$ of the external and internal meshing are the maximum values of all planetary gears, which can be calculated separately as follows:

$$
\begin{cases}
B_{spj} = \max_{1 \le i \le n} (B_{spij}) \\
B_{rpj} = \max_{1 \le i \le n} (B_{rpij})
\end{cases}
\tag{20}
$$

The sun gear floats near its ideal central position because of the error excitation, and its radial floating displacement is as follows:

$$
\begin{cases}
X_{sj} = \cos(\omega_{sj}t)H_{sj} - \sin(\omega_{sj}t)V_{sj} \\
Y_{sj} = \sin(\omega_{sj}t)H_{sj} + \cos(\omega_{sj}t)V_{sj}
\end{cases}
\tag{21}
$$

## 3. Load Sharing Analysis of the Pitch Drive for a 2 MW Wind Turbine

### 3.1. The Pitch Drive of a 2 MW Wind Turbine

The example analyzed in this study is the pitch drive with a three-stage planetary gear system in a 2 MW wind turbine. The main function of the pitch drive serves as pitching and adjusting the output power of the wind turbine. Its parameters are listed in Table 2. There are three planetary gears equally placed in each stage, and the phase angle of first planetary gear is $2\pi/3$.

**Table 2.** Parameters of the pitch drive of a 2 MW wind turbine.

| Parameters | First Stage | Second Stage | Third Stage |
|---|---|---|---|
| Sun gear tooth number | 12 | 18 | 16 |
| Planetary gear tooth number | 30 | 28 | 23 |
| Ring gear tooth number | 75 | 75 | 65 |
| Module | 2.5 | 2.5 | 4 |
| Mass of carrier (kg) | 2.28 | 4.15 | 13.98 |
| External meshing angle $\alpha_w$ (°) | 26.24 | 22.54 | 26.07 |
| Internal meshing angle $\alpha_n$ (°) | 16.04 | 19.32 | 14.69 |
| Input power P (kw) | | 6.4 | |
| Input speed $n_s$ (r/min) | 1600 | 220.7 | 42.7 |

In the first stage, the sun gear is applied by an external torque from the driving motor, so it only has a rotational movement, and $H_{s1}$ and $V_{s1}$ are zero. Each planetary gear and carrier has the lateral, vertical and rotational movements, and the ring gear in every stage is fixed by the flange. Thus, there are 13 degrees of freedom in the first stage.

In addition, each of the sun gears, the planetary gear and the carrier in the second and third stage, has three degrees of freedom; there are 15 degrees of freedom in the second or third stage with three planetary gears. As a result, there are a total of 43 degrees of freedom in dynamic load sharing model of pitch drive.

The supporting and meshing stiffness in all stages are listed in Table 3, and the values of the considered errors are shown in Table 4.

**Table 3.** Stiffnesses for all stages (N/m).

| Parameters | First Stage | Second Stage | Third Stage |
|---|---|---|---|
| Carrier support stiffness | $1.5 \times 10^9$ | $1.52 \times 10^9$ | $1.7 \times 10^9$ |
| Carrier rotational stiffness | $1.3 \times 10^9$ | $1.32 \times 10^9$ | $1.41 \times 10^9$ |
| Average external meshing stiffness | $8.16 \times 10^8$ | $2.09 \times 10^9$ | $3.17 \times 10^9$ |
| Average internal meshing stiffness | $1.11 \times 10^9$ | $2.52 \times 10^9$ | $3.91 \times 10^9$ |

### 3.2. Dynamic Load Sharing Coefficient

The load sharing coefficients of the internal and external meshing in three stages calculated based on the model above are shown in Figure 4a–f, respectively. The dynamic load sharing coefficients vary periodically with the gears operation. In the first stage, the dynamic load sharing coefficient $B_{sp1}$ of the external meshing is 1.076 and $B_{rp1}$ of the internal meshing is 1.116. Then, $B_{sp2}$ of the external meshing is 1.016 and $B_{rp2}$ of the internal meshing is 1.028 in the second stage. Moreover, the dynamic load sharing coefficient $B_{sp3}$ is 1.092 and $B_{rp3}$ of the internal meshing is 1.027 in the third stage.

**Table 4.** The errors of the transmission component in the pitch drive.

| Error | First Stage (µm) | Second Stage (µm) | Third Stage (µm) |
|---|---|---|---|
| $E_s$ | $(17, 0°)$ | $(17, 0°)$ | $(22, 0°)$ |
| $E_{pi}$ | $(21, 0°) (21, 120°)$ $(21, 240°)$ | $(21, 0°) (21, 120°)$ $(21, 240°)$ | $(21, 0°) (21, 120°)$ $(21, 240°)$ |
| $E_I$ | $(40, 0°)$ | $(40, 0°)$ | $(41, 0°)$ |
| $E_c$ | $(25, 0°)$ | $(25, 0°)$ | $(25, 0°)$ |
| $A_I$ | $(20, 0°)$ | $(20, 0°)$ | $(30, 0°)$ |
| $\varepsilon_{spi}$ | 15 | 15 | 15 |
| $\varepsilon_{piI}$ | 20 | 20 | 20 |



(**a**)



(**b**)



(**c**)



(**d**)



(**e**)



(**f**)
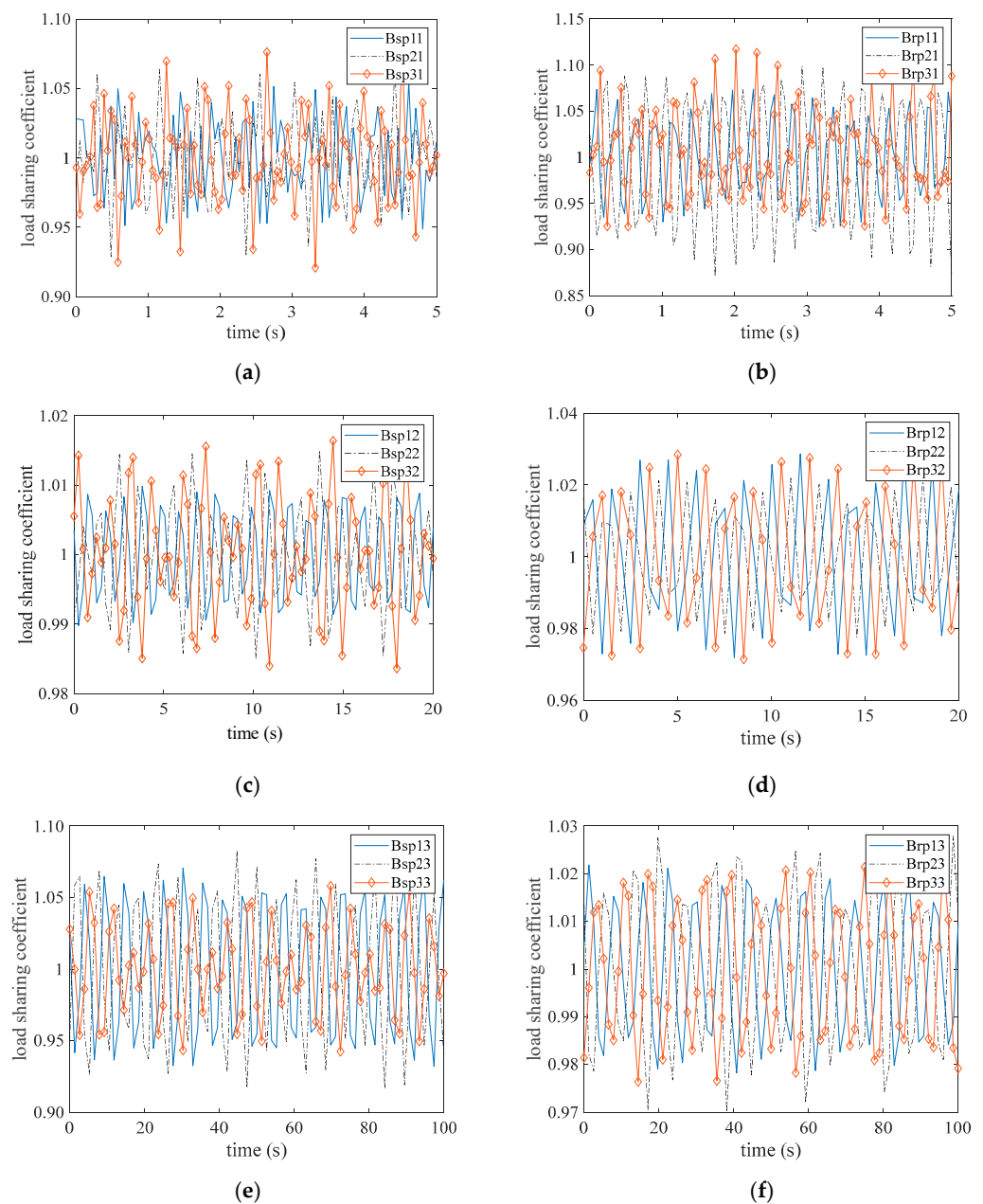
**Figure 4.** The load sharing coefficients for the internal and external meshing in all stages. (**a**) External meshing in the first stage; (**b**) internal meshing in the first stage; (**c**) external meshing in the second stage; (**d**) internal meshing in the second stage; (**e**) external meshing in the third stage; (**f**) internal meshing in the third stage.

### 3.3. Floating Displacement of the Sun Gear

The sun gear deviates from the original position with fluctuation. As the sun gear in the first stage of the pitch drive of wind turbines is radially fixed, it cannot float. As a consequence, only the floating displacement of sun gears in the second and third stage is researched in this study. The longitudinal and lateral floating displacements in the second and third stage are shown in Figure 5a,b, respectively. The radial synthetic floating displacement of the sun gear is 0.028 mm in the second stage and 0.087 mm in the third stage.



(a)

(b)
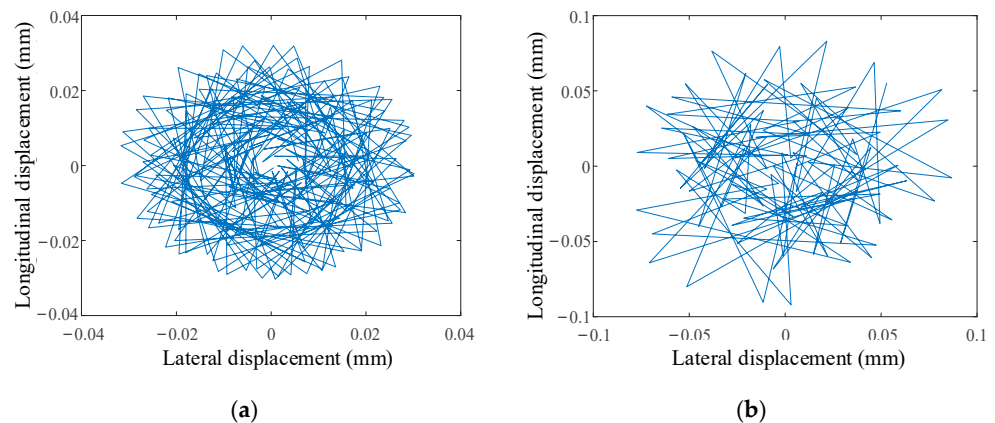
**Figure 5.** Floating displacement of the sun gear. (a) The second stage; (b) the third stage.

### 3.4. Dynamic Displacement of the Gears

The time-domain displacement of each component in each stage is analyzed in this section. The time-domain displacement of the components in certain directions in the first, second and third stage are shown in Figures 6–8, respectively. Owing to the rotation torque in every stage, the rotational displacement of the planetary gear is larger than its radial displacement. Additionally, the displacement of the sun gear, the planetary gear and the carrier in the third stage is greater than that in the first and second stages, on account of the largest torque in the third stage.



(a)

(b)

(c)

(d)
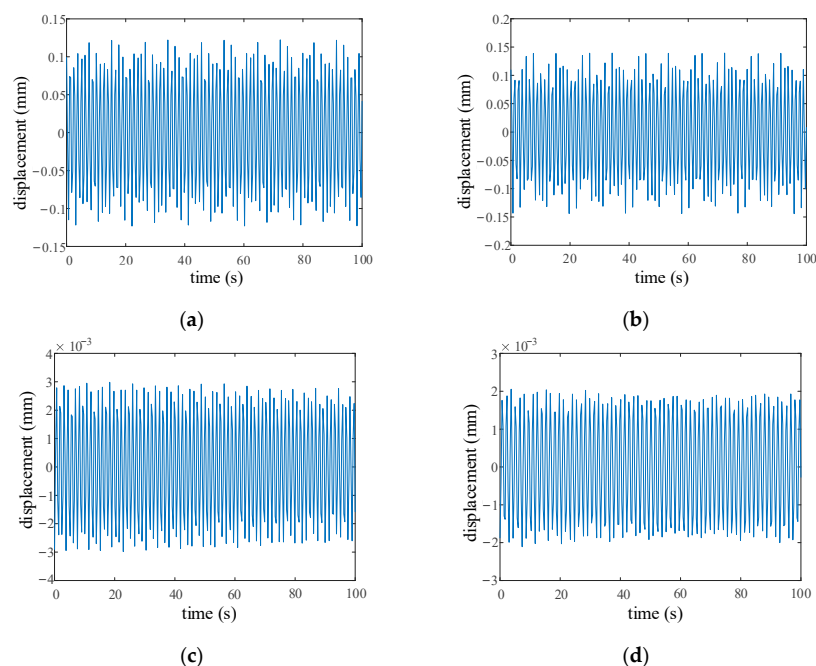
**Figure 6.** The time domain response of some components in the first stage. (a) Rotational displacement $u_{p11}$ of the planetary gear; (b) rotational displacement $u_{p31}$ of the planetary gear; (c) radial displacement $\eta_{p31}$ of the planetary gear; (d) horizontal displacement $X_{c1}$ of the carrier.
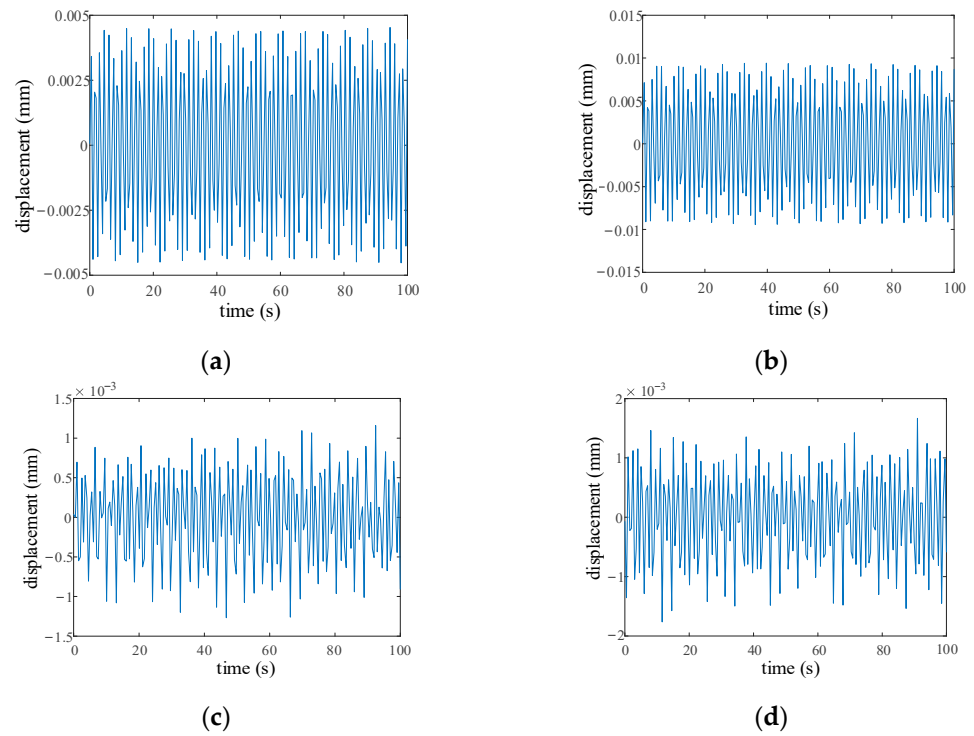
**Figure 7.** The time domain response of some components in the second stage. (**a**) Rotational displacement $u_{p12}$; (**b**) rotational displacement $u_{p22}$; (**c**) radial displacement $\eta_{p22}$; (**d**) horizontal displacement $X_{c2}$ of the carrier.
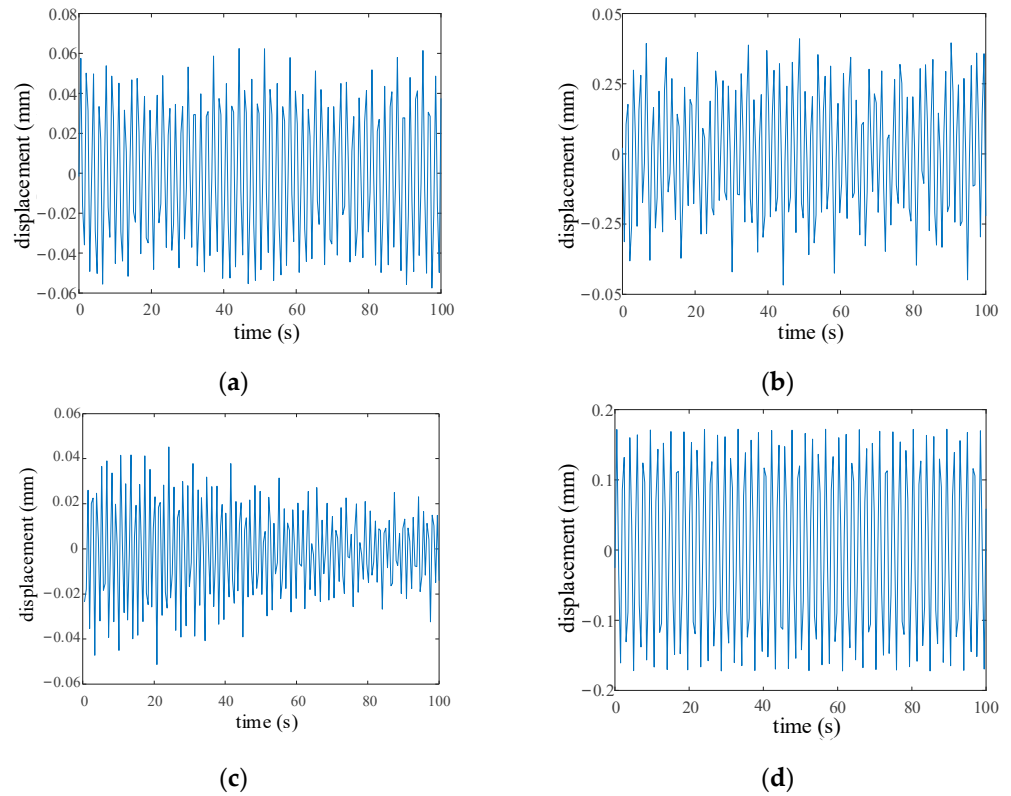


**Figure 8.** The time domain response of some components in the third stage. (**a**) Horizontal displacement $H_{s3}$; (**b**) rotation displacement $u_{p33}$; (**c**) vertical displacement $Y_{c3}$ of the carrier; (**d**) rotation displacement $u_{c3}$ of the carrier.

### 3.5. The Displacement of Carrier under Different Loads

In order to analyze displacement under different loads, the displacement of the carrier in the third stage under 50% and 150% rated torque are also calculated in the time-domain. The vertical displacement $Y_{c3}$ of the carrier in the third stage under 50% and 150% rated torque are shown in Figure 9a,b, respectively. In addition, the vertical displacement $Y_{c3}$ of the carrier under the rated torque is shown in Figure 8c. It can be seen from these figures that the displacement of the carrier improves slowly with the load increment.



(**a**)                    (**b**)
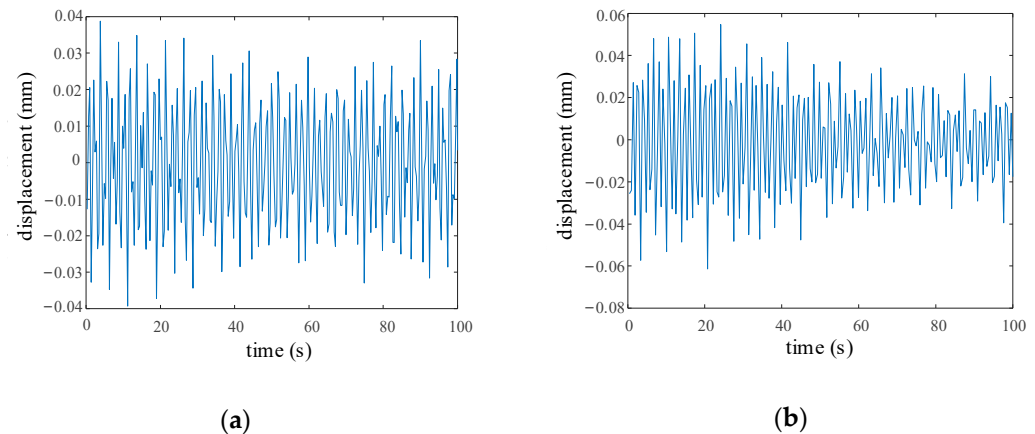
**Figure 9.** The time domain response of the carrier in the third stage under different loads. (**a**) Vertical displacement $Y_{c3}$ of the carrier under 50% load; (**b**) vertical displacement $Y_{c3}$ of the carrier under 150% load.

### 3.6. Analysis of the Parameter Sensitivity

#### 3.6.1. The Effect of the Meshing Stiffness on the Load Sharing Coefficient

The effect of external and internal meshing stiffness on the dynamic load sharing coefficient for the external and internal meshing in three stages of pitch drive is shown in Figure 10a–f, respectively. The time-varying meshing stiffness is replaced by the average meshing stiffness in this study. In the first stage, as external meshing stiffness increase, the dynamic load sharing coefficient of the internal meshing increases slowly but dynamic load sharing coefficient of the external meshing grows more significantly, as Figure 10a shows. For the internal meshing stiffness in Figure 10b, when the internal meshing stiffness turns to $8 \times 10^9$ N/m, the load sharing coefficient of the external meshing increases slightly. However, the load sharing coefficient of the internal meshing rises largely with the improvement in the internal meshing stiffness.

In the second and third stages, all the load sharing coefficients are under the impact of the saltation when the external and internal meshing stiffness reaches a specific value, as shown in Figure 10c–f, respectively.

The load sharing coefficients for each stage increase rapidly to the maximum and then gradually decrease and tend to be stable. In the second stage, the load sharing coefficients for the external and internal meshing are similar except for the saltation area. In the third stage, the load sharing coefficients of the external meshing are greater than those of the internal meshing as the stiffness of meshing increases. Therefore, both the internal and external meshing stiffness in the saltation areas should be avoided in the process of gear system design.

#### 3.6.2. The Effect of Eccentric Error on the Load Sharing Coefficient

The impact of the eccentric error of all components on the load sharing coefficients of the external and internal meshing in the first stage is shown in Figure 11a–d, noting that results for other stages are the same as in the first stage.

With eccentric error increment of the sun gear, the load sharing coefficient of the external meshing augments significantly. The load sharing coefficient of the internal meshing remains unchanged because the sun gear does not get incorporated into the internal meshing. Similar to the sun gear, the eccentric error of the ring gear has an obvious effect on the internal meshing, as shown in Figure 11a,b.
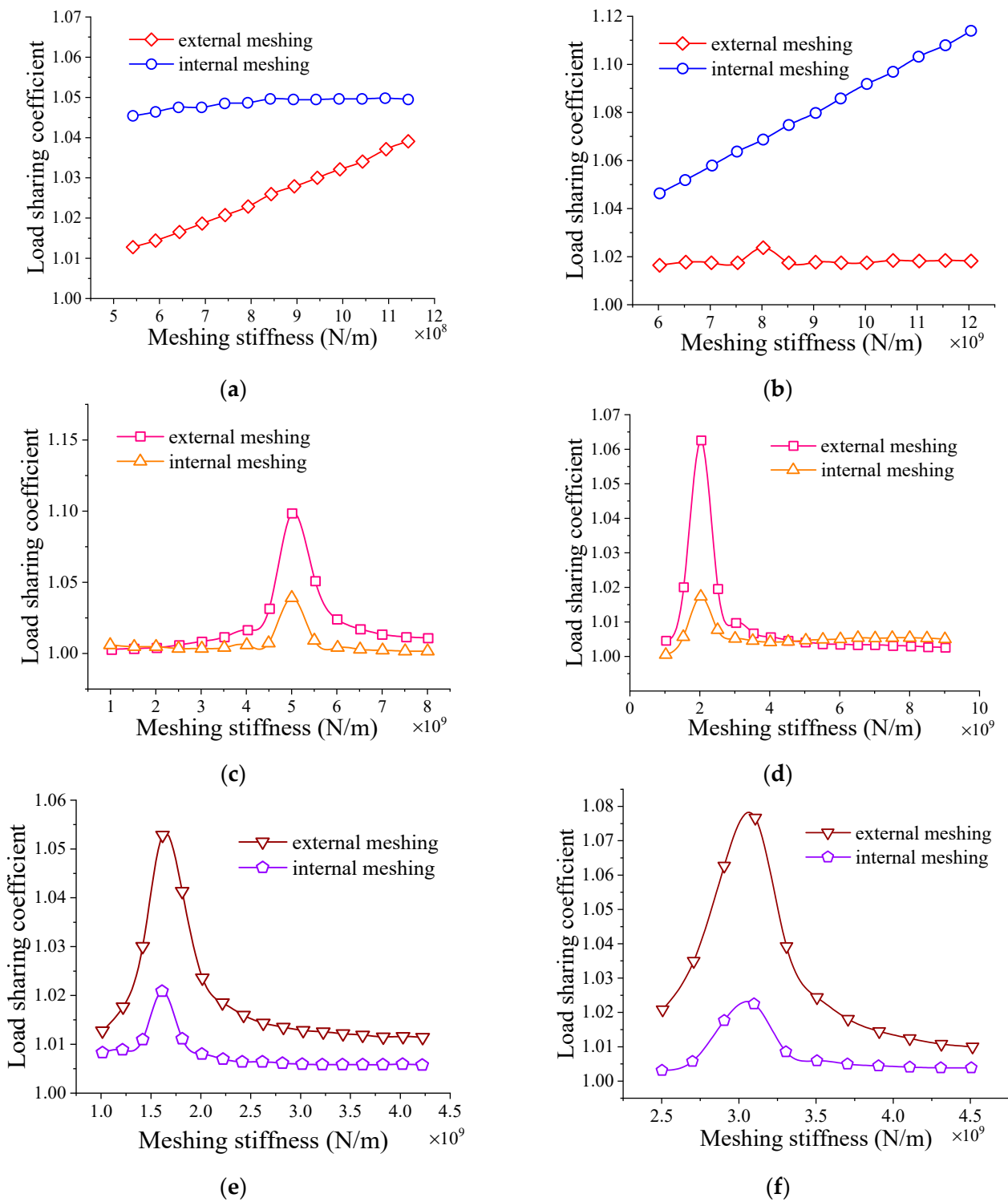
**Figure 10.** The effect of the meshing stiffness on the dynamic load sharing coefficient. (**a**) External meshing stiffness in the first stage; (**b**) internal meshing stiffness in the first stage; (**c**) external meshing stiffness in the second stage; (**d**) internal meshing stiffness in the second stage; (**e**) external meshing stiffness in the third stage; (**f**) internal meshing stiffness in the third stage.
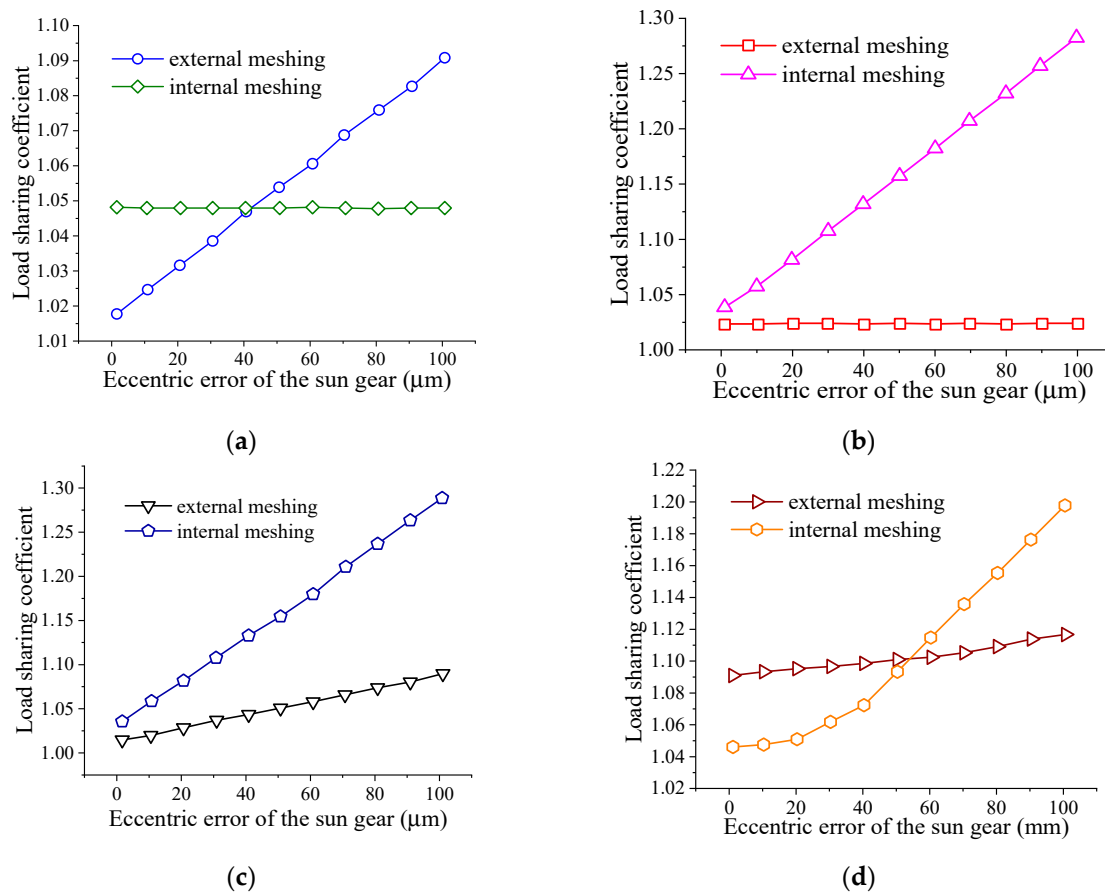
**Figure 11.** The effect of the eccentric error on the load sharing coefficient. (**a**) Eccentric error of the sun gear; (**b**) eccentric error of the ring gear; (**c**) eccentric error of the planetary gear; (**d**) eccentric error of the carrier.

Moreover, the load sharing coefficients of both the internal and external meshing augment with eccentric error increment of the planetary gear and the carrier, as shown in Figure 11c,d. Therefore, the eccentric error of the two components should be effectively controlled to improve the load sharing behavior of the system.

### 3.6.3. The Effect of Tooth Frequency Error on the Load Sharing Coefficient

The impact of the tooth frequency error on the load sharing coefficient of the external and internal meshing in three stages is shown in Figure 12a–f. In the first stage, the dynamic load sharing coefficient of the external meshing increases slowly with an augment in the tooth frequency error of the external meshing, while that of the internal meshing remains unchanged. When the tooth frequency error of the internal meshing grows, the dynamic load sharing coefficient of the internal meshing also improves significantly, while that of the external meshing is basically unchanged, as shown in Figure 12a,b. The influence of the tooth frequency error in the second stage is shown in Figure 12c,d. Both the load sharing coefficients of the external and internal meshing promote gradually as the tooth frequency error augments.

However, in the third stage, the load sharing coefficient of the external meshing augments dramatically with the tooth frequency error for the external meshing increasing, but it remains unchanged as with the increment of the tooth frequency error of the internal meshing. In addition, the load sharing coefficients for meshing do not change with the variation of the tooth frequency error of the both meshing.

It can be seen that the tooth frequency error of the external meshing bears more impact on the external meshing load sharing, and the tooth frequency error of the internal meshing mainly affects the internal meshing load sharing, while sometimes the error of both the external and internal meshing interacts.
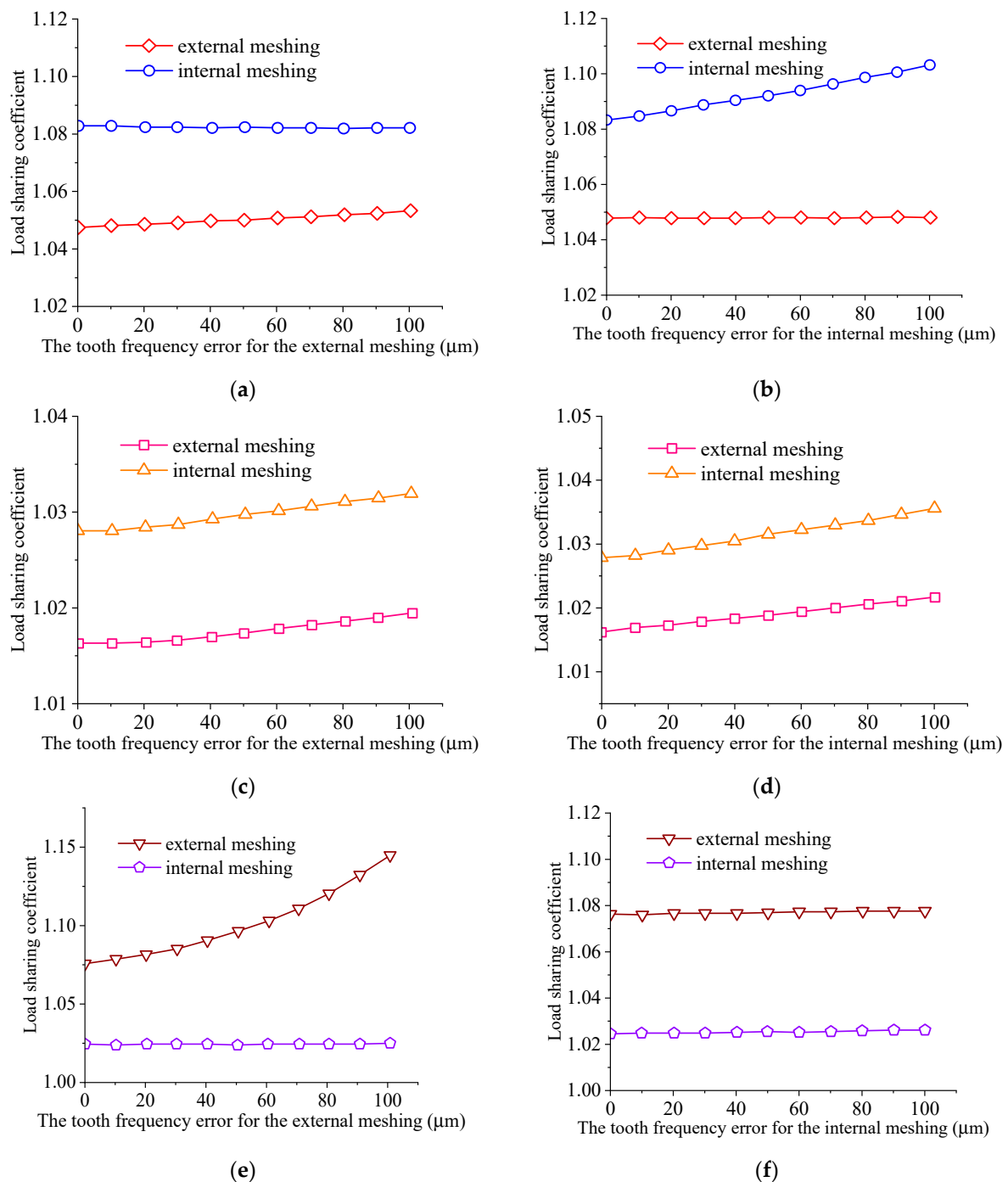
**Figure 12.** The effect of the tooth frequency error on the load sharing coefficient. (**a**) The external meshing in the first stage; (**b**) the internal meshing in the first stage; (**c**) the external meshing in the second stage; (**d**) the internal meshing in the second stage; (**e**) the external meshing in the third stage; (**f**) the internal meshing in the third stage.

## 4. Dynamics Experiments of Pitch Drive

### 4.1. Test Rig of Pitch Drive

A test rig is built to measure the dynamics behavior of the pitch drive of 2 MW wind turbines. The structure of the pitch drive is shown in Figure 13. Additionally, as shown in Figure 14a, the tested pitch drive connects with an accompanied gearbox through an idle gear with the input speed 1600 r/min and input power 6.4 KW. The power is supplied by a direct current motor equipped with electronic speed control, and then transmitted to the tested gearbox, idler and the accompanied

gearbox. The rotational speed decreases through the tested gearbox and then increases through the accompanied gearbox. A torque speed sensor is installed between the motor and gearbox.

Furthermore, a uniaxial vibration sensor is mounted on the output shaft housing of the tested gearbox through magnetic attraction. The vibration sensor is Vib 90 with a 1000 Hz frequency response; it tests the radial acceleration signal of the output shaft. A signal processor inside the vibration sensor can calculate the velocity and displacement according to the vibration signal automatically, and then output the vibration data in the time domain. In addition, a data acquisition card is installed in the control cabinet. All the data are collected using LabView software and then displayed on the screen of the control cabinet, as shown in Figure 14b. Moreover, the vibration displacements of the gearbox are tested under three types of load: 50% rated torque, 100% rated torque and 150% rated torque.
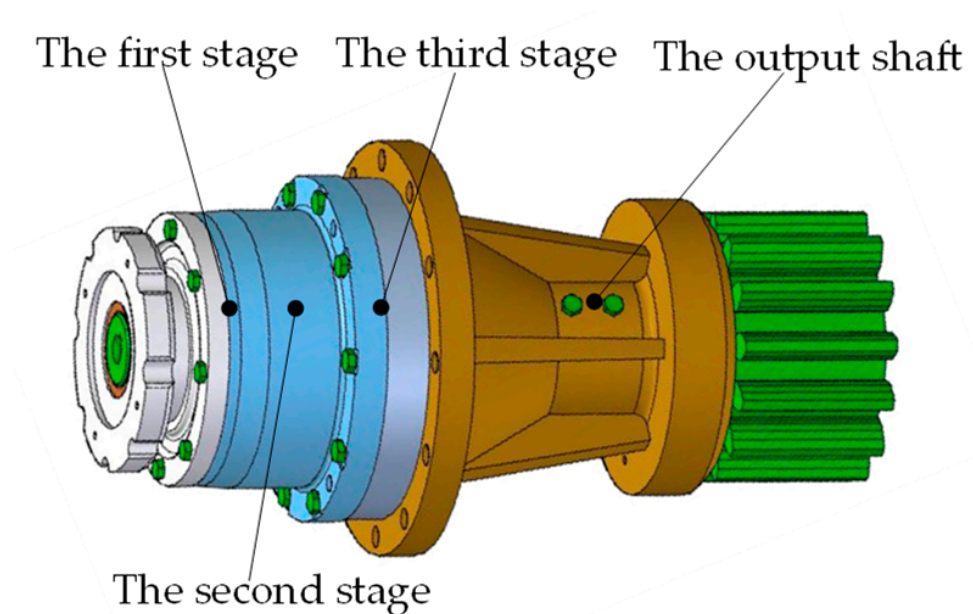


**Figure 13.** The structure of the pitch drive.
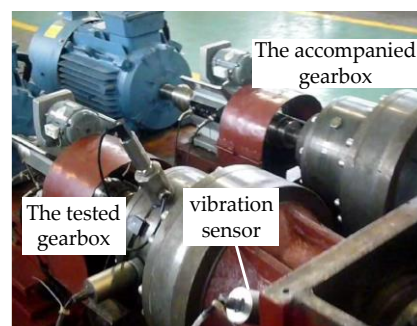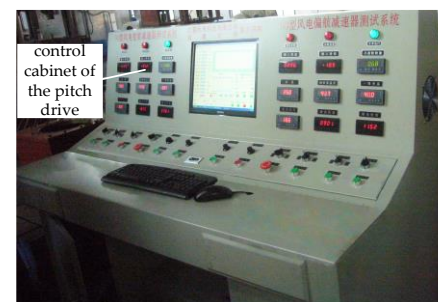


(**a**)　　　　　　　　　　　　　　　　　　　　　　　　　　　　　(**b**)

**Figure 14.** The test rig of the pitch drive. (**a**) Test rig; (**b**) control cabinet.

### 4.2. Experimental Results

Since the carrier in the third stage is connected to the output shaft, their displacements are similar. Thus, the displacement of the carrier in the third stage is replaced by that of the output shaft. The vibration displacements of the carrier in the third stage under 50%, 100% and 150% torque are shown in Figure 15a–c, respectively. The amplitude of the vibration displacement under 50% load is 0.043 mm, and the peak-to-peak displacement is 0.085 mm. Moreover, the amplitude of the vibration displacement with 100% load is 0.054 mm, and the peak-to-peak displacement is 0.105 mm. While the amplitude and the peak-to-peak displacement of the displacement for the carrier with 150% load are 0.063 mm and 0.121 mm, respectively.
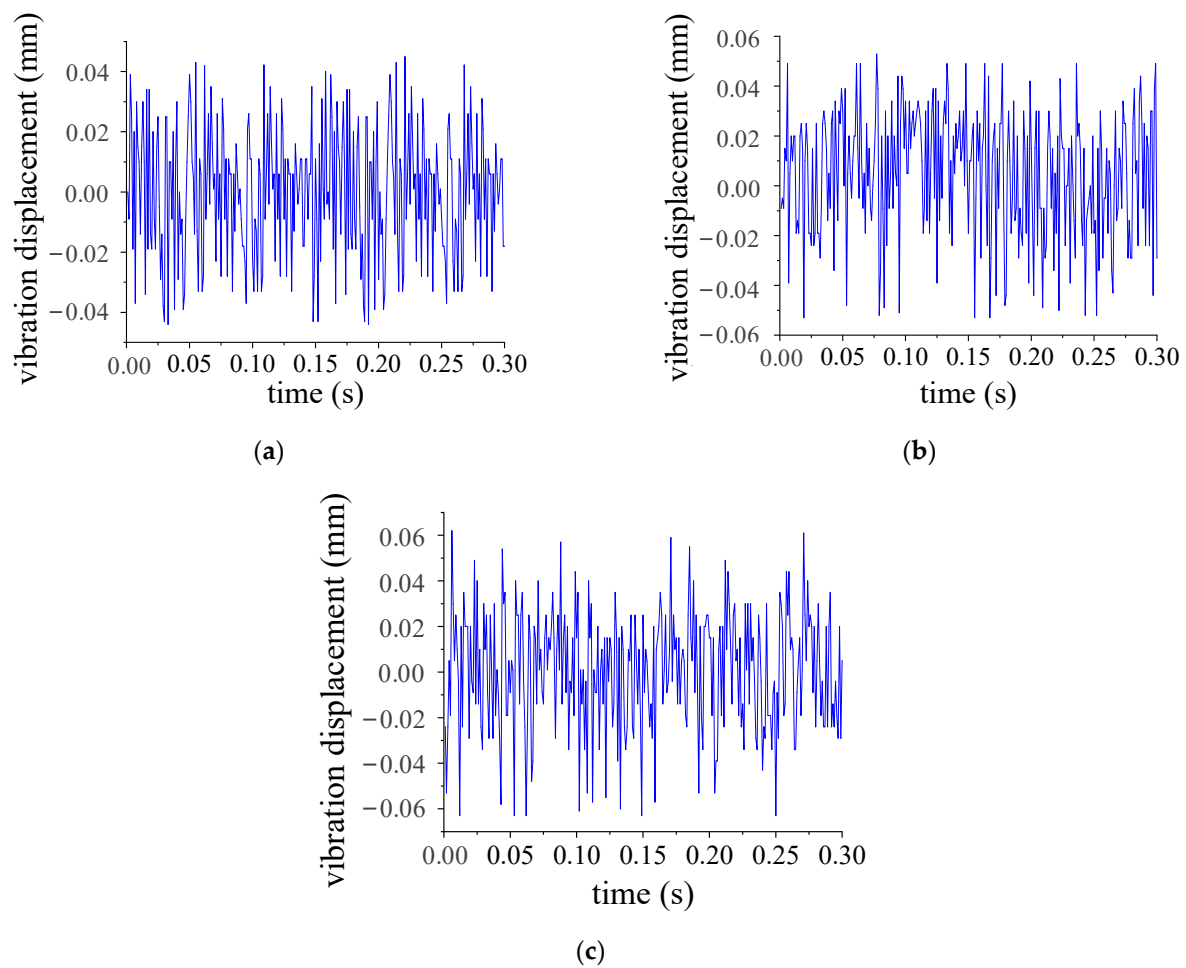
(**a**)

(**b**)



(**c**)

**Figure 15.** The vibration displacement of the carrier in the third stage. (**a**) Vibration displacement at 50% load; (**b**) vibration displacement at 100% load; (**c**) vibration displacement at 150% load.

*4.3. Comparison with Experimental Results*

Table 5 shows the comparison between the tested displacement and theoretical vertical displacement $Y_{c3}$ of the carrier in the third stage, which is shown in Figures 8c and 9a,b. Both the amplitude and peak-to-peak displacement of the theoretical displacement are close to those of the tested displacement. The experimental results generally agree with the theoretical results. The slight difference between the experiment and theoretical results may be because the magnetic attraction installation brings a small error. The effectiveness of the dynamic load sharing model for the pitch drive for MW wind turbines is validated.

**Table 5.** Comparison between the analytical and test vibration of the carrier in the third stage.

| Displacement | Method | 50% Torque | 100% Torque | 150% Torque |
|---|---|---|---|---|
| Amplitude (mm) | analytical | 0.039 | 0.051 | 0.061 |
| | test | 0.043 | 0.054 | 0.063 |
| Peak-to-peak | analytical | 0.078 | 0.097 | 0.116 |
| displacement (mm) | test | 0.085 | 0.105 | 0.121 |

**5. Conclusions**

This study investigates the load sharing of the pitch drive for MW wind energy systems, illustrates the dynamic load sharing model, and obtains the dynamic load sharing coefficients of all stages. Afterwards, the displacement calculated in this model is verified by an experiment, and the theoretical model is effective. Conclusions are achieved as follows:

1. The load sharing coefficient of external meshing in the first stage is the largest. Thus, the load distribution is most uneven in the first stage.
2. The effect of the external and internal meshing stiffness for all stages is studied with the basic parameters of the pitch drive of 2 MW wind turbines. There is saltation of the load sharing coefficient with the improvement in the meshing stiffness. Therefore, the meshing stiffness in the saltation areas should be avoided in the design process.
3. Furthermore, eccentric errors for the sun gear, carrier, ring gear and planetary gear on the load sharing behavior are analyzed in this paper. The load sharing coefficients of both internal and external meshing augment greatly with the increment of eccentric errors of the planetary gear and carrier. Therefore, these two errors should be controlled.
4. The tooth frequency error of the external/internal meshing bears a main impact on the corresponding load sharing coefficient.
5. The displacement of the dynamic load sharing model for the pitch drive in MW wind turbines is validated by the vibration experiment under the 50%, 100% and 150% rated torque in a test rig.

Lastly, these conclusions can provide a theoretical reference in designing high-performance planetary gear systems.

## References

1. Kahraman, A. Load Sharing Characteristics of Planetary Transmissions. *Mech. Mach. Theory* **1994**, *29*, 1151–1165. [CrossRef]
2. Iglesias, M.; Fernandez, A.; Dejuan, A. Planet position errors in planetary transmission: Effect on load sharing and transmission error. *Front. Mech. Eng.* **2013**, *8*, 80–87. [CrossRef]
3. Iglesias, M.; Fernandez, A.; Dejuan, A. Planet Eccentricity Error on a Planetary Gear Transmission: Influence on Load Sharing. *Mech. Mach. Sci.* **2015**, *21*, 1381–1390.
4. Iglesias, M.; Fernandez, A.; Dejuan, A. Planetary transmission load sharing: Manufacturing errors and system configuration study. *Mech. Mach. Sci.* **2017**, *11*, 21–38. [CrossRef]
5. Xu, Z.; Yu, W.; Shao, Y.; Yang, X.; Nie, C.; Peng, D. Dynamic modeling of the planetary gear set considering the effects of positioning errors on the meshing position and the corner contact. *Nonlinear Dyn.* **2022**, *109*, 1551–1569. [CrossRef]
6. Ryali, L.; Talbot, D. A dynamic load distribution model of planetary gear sets. *Mech. Mach. Theory* **2021**, *158*, 104229. [CrossRef]
7. Kim, J.G.; Park, Y.J.; Lee, G.H.; Lee, S.T.; Oh, J.Y. Experimental Study on the Carrier Pinhole Position Error Affecting Dynamic Load Sharing of Planetary Gearboxes. *Int. J. Precis. Eng. Manuf.* **2018**, *19*, 881–887. [CrossRef]
8. Kim, J.G.; Park, Y.J.; Lee, S.D.; Oh, J.Y.; Kim, J.H.; Lee, G.H. Influence of the Carrier Pinhole Position Errors on the Load Sharing of a Planetary Gear Train. *Int. J. Precis. Eng. Manuf.* **2018**, *19*, 537–543. [CrossRef]
9. Wang, J.; Yang, S.; Liu, Y.; Mo, R. Analysis of Load-Sharing Behavior of the Multistage Planetary Gear Train Used in Wind Generators: Effects of Random Wind Load. *Appl. Sci.* **2019**, *9*, 5501. [CrossRef]
10. Theling, J.; Brimmers, J.; Brecher, C. Reducing mass while improving the operational behavior: Form optimization of planetary gearbox housings. *Forsch. Im Ing.* **2021**, *85*, 543–551. [CrossRef]
11. Chung, W.-J.; Oh, J.-S.; Han, H.-W.; Kim, J.-T.; Park, Y.-J. Analytical study of floating effects on load sharing characteristics of planetary gearbox for off-road vehicle. *Adv. Mech. Eng.* **2020**, *12*, 1687814020940468. [CrossRef]

12. Fan, Z.; Zhu, C.; Song, C. Dynamic Analysis of Planetary Gear system Considering the Flexibility of Internal Ring Gear. *Iran. J. Sci. Technol. Trans. Mech. Eng.* **2020**, *44*, 695–706. [CrossRef]

13. Ryali, L.; Talbot, D. A dynamic gear load distribution model for epicyclic gear sets with a structurally compliant planet carrier. *Mech. Mach. Theory* **2023**, *181*, 105225. [CrossRef]

14. Park, Y.J.; Lee, G.H.; Oh, J.S.; Shin, C.S.; Nam, J.S. Effects of Non-torque Loads and Carrier Pinhole Position Errors on Planet Load Sharing of Wind Turbine Gearbox. *Int. J. Precis. Eng. Manuf. Green Technol.* **2019**, *6*, 281–292. [CrossRef]

15. Yoo, H.G.; Chung, W.J.; Kim, B.S.; Park, Y.J.; Kim, S.C.; Lee, G.H. Application of flexible pin for planetary gear set of wind turbine gearbox. *Sci. Rep.* **2022**, *12*, 1713. [CrossRef] [PubMed]

16. Zhu, Z.; Zhu, R.; Bao, H.; Jin, G. Impact of run-out and meshing-frequency errors on dynamic load sharing for encased differential herringbone train. *J. Aerosp. Power* **2011**, *26*, 2601–2609.

17. Chen, W.; Chen, S.; Hu, Z.; Tang, J.; Li, H. Dynamic analysis of a bevel gear system equipped with finite length squeeze film dampers for passive vibration control. *Mech. Mach. Theory* **2020**, *147*, 103779. [CrossRef]

18. Zhu, Z.; Zhu, R.; Bao, H.; Jin, G. Analysis of dynamic floating displacement of center gear for encased differential planetary train. *J. Cent. South Univ.* **2012**, *43*, 497–504.

19. Sun, Z.; Shen, Y.; Li, S. Study on dynamic behavior of encased differential gear train. *Chin. J. Mech. Eng.* **2002**, *38*, 44–52. [CrossRef]